Nonlinear Wavelength Selection in a Channel

P G Daniels[1], D Ho[1] and A C Skeldon[2]

[1] *Centre for Mathematical Science, City University, Northampton Square, London EC1V 0HB, UK*
[2] *Department of Mathematics and Statistics, University of Surrey, Guildford, Surrey GU2 7XH, UK*

A method is described for calculating nonlinear steady-state patterns in channels taking into account the effect of an end wall across the channel. The key feature is the determination of the phase shift of the nonlinear periodic form distant from the end wall as a function of wavelength. This is found by analysing the solution close to the end wall, where Floquet theory is used to describe the departure of the solution from its periodic form and to locate the Eckhaus stability boundary. A restricted band of wavelengths is identified, within which solutions for the phase shift are found by numerical computation in the fully nonlinear regime and by asymptotic analysis in the weakly nonlinear regime. Results are presented here for the two-dimensional Swift-Hohenberg equation but in principle the method can be applied to more general pattern-forming systems. Near onset, it is shown that for channel widths less than a certain critical value the restricted band includes both subcritical and supercritical wavelengths, whereas for wider channels only subcritical wavelengths are allowed.
Key words: convection; nonlinear systems; pattern selection.

1 Introduction

There are many examples of systems that develop a cellular pattern through a bifurcation or smooth evolution from a structureless state. Such patterns have been observed in the hydrodynamic instability of fluids, such as Rayleigh-Benard convection and Taylor-Couette flow, in solidification processes, plate buckling, nonlinear optics, and in chemical and biological systems (see, for example, Cross & Hohenberg 1993). In many technological applications, such as crystal growth processes, solar collectors and heat exchangers, motion occurs within a channel-like geometry and is strongly influenced by the sidewalls and end walls of the channel. Carefully controlled Rayleigh-Benard experiments in long channels (Kirchartz & Oertel 1988) show that cellular patterns consisting of convection rolls parallel to the end walls can be subject to significant variations in wavelength as the Rayleigh number increases above its threshold value. Such variations affect the heat transfer characteristics of the system and are therefore of interest in applications of the kind mentioned above. Numerical simulations of the entire flow are hampered by the immense computing power needed to accurately simulate three-dimensional

convection (Arter & Newell 1988) and the main objective of the present work is to develop a method that will allow wavelength selection to be predicted in the fully nonlinear regime without the need for such extensive simulations.

A number of phenomenological models have been studied as a means of gaining insight into the nonlinear regime. The following model equation was first introduced by Swift & Hohenberg (1977):

$$\frac{\partial u}{\partial t} = \epsilon u - (1 + \nabla^2)^2 u - u^3. \tag{1}$$

Here t is time, x and y are horizontal spatial variables, $\nabla^2 = \partial^2/\partial x^2 + \partial^2/\partial y^2$, ϵ is a control parameter and $u = u(x, y, t)$ is a two-dimensional scalar field which represents a characteristic property of the pattern, such as the vertical velocity component at mid-height in a convecting fluid layer. Cross et al (1983) investigated the effect of lateral boundaries on solutions of the one-dimensional equation in the weakly nonlinear regime ($\epsilon \ll 1$). They showed that even if the lateral walls are far (many roll widths) apart, they severely restrict the band of allowed wavenumbers in the bulk of the fluid compared with that which exists for the corresponding infinite layer. These results were extended to two values of ϵ in the nonlinear regime by Kramer & Hohenberg (1984) and to a range of values of ϵ by Daniels et al (2003) who showed how the waveband is related to the phase shift of the periodic form relative to the wall. In the present paper this analysis is extended to the two-dimensional Swift-Hohenberg equation for a channel $-a \leq y \leq a$ with the equivalent of no-slip boundary conditions on the sidewalls:

$$u = \frac{\partial u}{\partial y} = 0 \text{ at } y = \pm a. \tag{2}$$

The plan of the paper is as follows. In section 2, periodic solutions in an infinite channel $-\infty < x < \infty$ are considered. Linear theory is used to determine the critical value ϵ_0 of ϵ above which spatially periodic solutions exist and these solutions are then found in both the weakly nonlinear regime ($\epsilon - \epsilon_0 \ll 1$) and the fully nonlinear regime ($\epsilon > \epsilon_0$). Floquet analysis is used in section 3 to study spatial perturbations to these periodic solutions and to determine the Eckhaus stability boundary. This leads to the consideration in section 4 of solutions for a semi-infinite channel $x \geq 0$ with an end wall where

$$u = \frac{\partial u}{\partial x} = 0 \text{ at } x = 0. \tag{3}$$

The Floquet analysis determines the spatial decay that occurs in order for the boundary conditions at the end wall to be met. As in the one-dimensional case, it is found that steady-state solutions exist for a restricted band of wavelengths. Within this band the phase shift of the periodic form relative to the end wall is determined as a function of wavelength using numerical computation in the fully nonlinear regime and asymptotic analysis in the weakly nonlinear regime. Finally,

in section 5, a discussion is given of how the present method can be extended to solve the equivalent nonlinear Rayleigh-Benard system in long channels where, so far, theoretical results are limited to the solution of the linear problem with various conditions on the channel walls (Davies-Jones 1970, Luijkx & Platten 1981, Chana & Daniels 1989) and certain aspects of the weakly nonlinear problem with either stress-free horizontal walls (Daniels & Chana 1987) or no-slip horizontal walls (Daniels & Ong 1990).

2 Periodic solutions

In this section steady-state periodic solutions are found for an infinite channel $-\infty < x < \infty, -a \leq y \leq a$. Linear analysis is used to find the marginal stability curves that mark the onset of such solutions, weakly nonlinear analysis establishes their form close to onset and then fully nonlinear solutions are computed using a Fourier decomposition.

2.1 Linear analysis

Small perturbations from the trivial solution $u = 0$ are governed by the linearized version of (1), leading to steady-state solutions of the form

$$u = e^{iqx} f(y) + \text{c.c.}, \tag{4}$$

where q is the wavenumber along the channel, c.c. denotes complex conjugate and f satisfies

$$f'''' + 2(1-q^2)f'' + ((1-q^2)^2 - \epsilon)f = 0; \quad f = f' = 0 \quad (y = \pm a). \tag{5}$$

The channel halfwidth a can be removed through the transformations

$$y = aY, \quad f(y) = F(Y), \quad q^2 = 1 - Qa^{-2}, \quad \epsilon = \delta a^{-4}, \tag{6}$$

giving the system

$$F'''' + 2QF'' + (Q^2 - \delta)F = 0; \quad F = F' = 0 \quad (Y = \pm 1), \tag{7}$$

which depends only on the modified wavenumber Q and on δ. Solutions that are even about $Y = 0$ onset first and with a normalization $F(0) = 1$ have the form

$$F = \frac{\cos\bar{\mu}\cosh\mu Y - \cosh\mu\cos\bar{\mu}Y}{\cos\bar{\mu} - \cosh\mu}, \tag{8}$$

where

$$\mu = (\delta^{1/2} - Q)^{1/2}, \quad \bar{\mu} = (\delta^{1/2} + Q)^{1/2} \tag{9}$$

and

$$\mu\tanh\mu = -\bar{\mu}\tan\bar{\mu}. \tag{10}$$

Equation (10) defines the marginal stability curves in the Q, δ plane, the lowest two of which are shown in Fig.1. Turning points occur where $\mu \tanh \mu = 1$, with the lowest minimum at $(\mu, \bar{\mu}) = (\mu_0, \bar{\mu}_0) = (1.200, 2.798)$ corresponding to $(Q, \delta) = (Q_0, \delta_0) = (3.196, 21.48)$ and thus critical values of the wavenumber and control parameter given by

$$q_0 = (1 - 3.196a^{-2})^{1/2}, \quad \epsilon_0 = 21.48a^{-4}. \tag{11}$$

The effect of the channel walls is to inhibit the onset of instability: the narrower the channel the higher the value of ϵ_0. Note that in practice the minimum occurs at finite wavelengths only for sufficiently wide channels ($a > 1.788$). Fig.2 shows the variation of the profile $F(Y)$ for increasing values of Q on the lowest even branch. Odd solution branches are found from the equation $\mu \coth \mu = \bar{\mu} \cot \bar{\mu}$ and the lowest two of these are also shown in Fig.1.

2.2 Weakly nonlinear analysis $\epsilon - \epsilon_0 \ll 1$

The linear analysis shows that, as ϵ increases, steady-state periodic solutions with small amplitude first exist in the neighbourhood of the critical point ϵ_0 with wavenumber q_0. Locally the steady-state solution for u can be developed in the form

$$u = \bar{\epsilon}^{1/2} u_0 + \bar{\epsilon} u_1 + \bar{\epsilon}^{3/2} u_2 + \bar{\epsilon}^2 u_3 + \ldots, \quad \bar{\epsilon} \to 0, \tag{12}$$

where $\bar{\epsilon} = \epsilon - \epsilon_0 > 0$ and $u_i = u_i(x, y, X)$ are functions of x, y and the long length scale $X = \bar{\epsilon}^{1/2} x$. Substitution into (1) then yields in succession

$$\mathcal{L} u_0 \equiv \left(\left(1 + \frac{\partial^2}{\partial x^2} + \frac{\partial^2}{\partial y^2} \right)^2 - \epsilon_0 \right) u_0 = 0, \tag{13}$$

$$\mathcal{L} u_1 = -4 \left(1 + \frac{\partial^2}{\partial x^2} + \frac{\partial^2}{\partial y^2} \right) \frac{\partial^2 u_0}{\partial x \partial X}, \tag{14}$$

$$\mathcal{L} u_2 = -2 \left(1 + \frac{\partial^2}{\partial x^2} + \frac{\partial^2}{\partial y^2} \right) \left(2 \frac{\partial^2 u_1}{\partial x \partial X} + \frac{\partial^2 u_0}{\partial X^2} \right) - 4 \frac{\partial^4 u_0}{\partial x^2 \partial X^2} + u_0 - u_0^3. \tag{15}$$

The relevant solution of (13) is

$$u_0 = (A_0(X) e^{i q_0 x} + A_0^*(X) e^{-i q_0 x}) f_0(y), \tag{16}$$

where A_0 is a complex amplitude function, an asterisk denotes the complex conjugate and $f_0(y) = F_0(Y)$ is the solution (8) at the critical point. It now follows from (14) that

$$u_1 = (A_1(X) e^{i q_0 x} + A_1^*(X) e^{-i q_0 x}) f_0(y) - i (A_0' e^{i q_0 x} - A_0'^* e^{-i q_0 x}) g_0(y), \tag{17}$$

where A_1 is a further complex amplitude function and $g_0(y) = \partial f / \partial q |_{\epsilon_0}$, the partial derivative of f viewed as a function of y and q at points on the neutral curve, evaluated at $\epsilon = \epsilon_0$. The relevant solution of (15) is then given by

$$\begin{aligned} u_2 = (A_2(X) e^{i q_0 x} + A_2^*(X) e^{-i q_0 x}) f_0(y) - i (A_1' e^{i q_0 x} - A_1'^* e^{-i q_0 x}) g_0(y) + \\ e^{i q_0 x} h(y, X) + e^{-i q_0 x} h^*(y, X) + (A_0^3 e^{3 i q_0 x} + A_0^{*3} e^{-3 i q_0 x}) h_0(y), \end{aligned} \tag{18}$$

where A_2 is a further complex amplitude function. A consistent solution for the function h requires that A_0 satisfies the amplitude equation

$$\alpha_1 A_0'' + \alpha_2 A_0 - \alpha_3 A_0^2 A_0^* = 0, \tag{19}$$

where the coefficients are real and given by

$$\alpha_1 = a q_0^2 \alpha_{10} + a^{-1}\alpha_{11}, \quad \alpha_2 = a\alpha_{20}, \quad \alpha_3 = a\alpha_{30}, \tag{20}$$

where

$$\alpha_{10} = 2.926, \quad \alpha_{11} = 0, \quad \alpha_{20} = 0.7674, \quad \alpha_{30} = 1.683. \tag{21}$$

Details of the derivation of (19)-(21) and of the solutions for g_0, h_0 and h are given in Appendix A.

Periodic solutions of the amplitude equation (19) have the form

$$A_0 = (\alpha_2/\alpha_3)^{1/2}(1 - \alpha_1\alpha_2^{-1}\Omega^2)^{1/2} e^{i\Omega X} \tag{22}$$

(to within an arbitrary origin shift in X) where $\Omega^2 < \alpha_2/\alpha_1$. Thus weakly nonlinear periodic solutions are confined to overall wavenumbers q in the range

$$q_0 - (\epsilon - \epsilon_0)^{1/2}(\alpha_2/\alpha_1)^{1/2} < q < q_0 + (\epsilon - \epsilon_0)^{1/2}(\alpha_2/\alpha_1)^{1/2} \tag{23}$$

which defines the marginal stability curve in the neighbourhood of $\epsilon = \epsilon_0$. Using (20) and (21), it follows that for general values of $a > 1.788$ the waveband of nonlinear solutions is restricted to wavelengths $2\pi/q$ bounded by

$$\frac{2\pi a}{(a^2 - 3.196)^{1/2}}\left(1 \pm \frac{0.5121 a^2 (\epsilon - \epsilon_0)^{1/2}}{a^2 - 3.196}\right) \tag{24}$$

as $\epsilon \to \epsilon_0$. For large channel widths ($a \to \infty$) this predicts a band of wavelengths of width $6.435(\epsilon - \epsilon_0)^{1/2}$ centred on the critical wavelength of 2π and with $\epsilon_0 = 0$. In the long wavelength limit $a \to 1.788+$, both the critical wavelength and the bandwidth increase, and the validity of formula (24) is restricted to a diminishingly small range of ϵ near ϵ_0, which approaches the value 2.104.

2.3 Nonlinear solutions

Fully nonlinear periodic solutions of (1) and (2) can be sought in the form

$$u = u_p(x, y) = \sum_{n=1}^{N} a_n(y) \sin nqx, \tag{25}$$

where q is the wavenumber. The value of N is infinite in general but in practice solutions can be found by truncating the infinite series. The form (25) can be generalized to incorporate an origin shift in x if required and allows the weakly

nonlinear solutions of section 2.2 to be extended to general values of $\epsilon > \epsilon_0$. Substitution of (25) into (1) gives

$$\sum_{n=1}^{N}\{a_n'''' + 2(1-n^2q^2)a_n'' + (n^4q^4 - 2n^2q^2 + 1 - \epsilon)a_n\}\sin nqx = -\Big\{\sum_{n=1}^{N} a_n \sin nqx\Big\}^3. \tag{26}$$

By comparing coefficients of $\sin nqx$ on each side, this leads to a coupled system of N fourth-order ordinary differential equations for the coefficients $a_n, n = 1, 2, \ldots N$ to be solved subject to the boundary conditions $a_n = a_n' = 0$ on $y = \pm a$, obtained from (2). This system was solved using finite difference approximations to the derivatives of a_n with a truncation error of order $(\Delta y)^2$ where Δy is the step length in y. This leads to a matrix equation $A\mathbf{a} = \mathbf{b}$ where A is the matrix containing all the coefficients arising from the linear terms in (26), $\mathbf{a}$ is the vector of unknown coefficients at equally-spaced intervals in y and $\mathbf{b}$ is a vector containing all contributions from the nonlinear terms on the right-hand side of (26). This system was solved by a Newton-Krylov iterative scheme, using the linear theory of section 2.1, together with a single-mode truncation ($N = 1$) to obtain initial results which were then used as starting values for higher truncation levels, up to $N = 9$. The scheme was implemented mostly with 51 equally-spaced locations in y and checks with other step sizes and with linear theory indicated good accuracy in this case.

Results for the case $a = \pi$ where, from (11), $q_0 = 0.8223$ and $\epsilon_0 = 0.2206$ are shown in Figs 3-5. Fig.3 shows the variation of the coefficients a_n with ϵ for $q = 1$ and $n = 1, 3, 5, 7, 9$. The even coefficients are zero, a consequence of the cubic nonlinearity in (26). The coefficients a_n decrease in size rapidly with n, so that only a few modes give a good approximation to the nonlinear solution for the values of ϵ under consideration here. Fig.4 shows the variation of the coefficient a_1 with y and the wavenumber q for $\epsilon = 0.5$. The solution vanishes at the wavenumbers corresponding to the neutral curve $q = 1.1022$ and $q = 0.3597$. Fig.5 shows the nonlinear periodic solution $u_p(x, y)$ defined by (25) as a function of both x and y for $q = 1$ and $\epsilon = 0.5$.

3 Floquet analysis and the Eckhaus boundary

Steady-state perturbations to the nonlinear periodic solutions determined in the previous section are now considered by writing

$$u = u_p(x, y) + \bar{k}\bar{u}(x, y), \tag{27}$$

where the constant $\bar{k}$ is small. Substitution into (1) and (2) and neglect of nonlinear terms in $\bar{k}$ shows that $\bar{u}$ satisfies

$$\frac{\partial^4\bar{u}}{\partial x^4} + \frac{\partial^4\bar{u}}{\partial y^4} + 2\frac{\partial^4\bar{u}}{\partial x^2 y^2} + 2\Big(\frac{\partial^2\bar{u}}{\partial x^2} + \frac{\partial^2\bar{u}}{\partial y^2}\Big) + (1-\epsilon)\bar{u} + 3u_p^2\bar{u} = 0 \tag{28}$$

with boundary conditions

$$\bar{u} = \frac{\partial \bar{u}}{\partial y} = 0 \text{ on } y = \pm a. \tag{29}$$

Equation (28) is a linear partial differential equation with coefficients periodic in x and it follows that a solution can be sought in the Floquet form

$$\bar{u} = e^{-cx} \sum_{n=0}^{\bar{N}} \Big(b_n(y) \cos nqx + c_n(y) \sin nqx \Big), \tag{30}$$

where c is the characteristic exponent and the periodic part of the solution is expressed as a Fourier series in x whose coefficients $b_n(y), n = 0, 1, \ldots$ and $c_n(y), n = 1, 2 \ldots$ are bounded functions of y. If c is complex then the conjugate of $\bar{k}\bar{u}$ can be added in (27) to obtain the real solution for u. The value of $\bar{N}$ is infinite in general but in practice solutions can be found by truncating the infinite series in both (30) and (25). For $\bar{N} = 1$ and $N = 1$ the equations for the coefficients b_0, b_1 and c_1 are determined from (28) as

$$b_0'''' + 2(1 + c^2) b_0'' + (c^4 + 2c^2 + 1 - \epsilon) b_0 = -3a_1^2 b_0/2, \tag{31}$$

$$\begin{aligned} b_1'''' + 2(1 + c^2 - q^2) b_1'' - 4qcc_1'' + 4qc(q^2 - c^2 - 1) c_1 \\ + (c^4 + 2(1 - 3q^2)c^2 + q^4 - 2q^2 + 1 - \epsilon) b_1 = -3a_1^2 b_1/4, \end{aligned} \tag{32}$$

$$\begin{aligned} c_1'''' + 2(1 + c^2 - q^2) c_1'' + 4qcb_1'' - 4qc(q^2 - c^2 - 1) b_1 \\ + (c^4 + 2(1 - 3q^2)c^2 + q^4 - 2q^2 + 1 - \epsilon) c_1 = -9a_1^2 c_1/4. \end{aligned} \tag{33}$$

The equation for b_0 is disjoint from those for b_1 and c_1. In fact, because $a_n = 0$ for even values of n, solutions for the Floquet coefficients are obtained either with $b_n = c_n = 0$ for odd n or with $b_n = c_n = 0$ for even n. Freedom in the choice of the imaginary part of c means that attention can be restricted to the latter case.

In view of the rapid convergence of (25), computations were carried out initially using the truncated system (32),(33) together with the boundary conditions $b_1 = b_1' = c_1 = c_1' = 0$ at $y = \pm a$ obtained from (29). The finite difference scheme of section 2 was used to discretize the system leading to a linear homogeneous matrix equation $B\mathbf{f} = \mathbf{0}$ for the discrete values of b_1 and c_1 at M equally-spaced locations in the y direction. Most computations were carried out with $M = 17$. Non-trivial solutions exist for a discrete set of values of the characteristic exponent c for which the determinant of the matrix B vanishes. Initially the values of a, q and ϵ were fixed and c was varied within the complex plane to find the zeros of the determinant of B. Generally this determinant is a very large complex function so to avoid truncation errors it was more convenient to search for zeros of the eigenvalue of minimum modulus, $\lambda_B = \min |\text{eig} B|$. Fig.6 shows contours of $\log \lambda_B$ in the range $-5 < \text{Re}(c) < 5, -5 < \text{Im}(c) < 5$ for the case $a = \pi, q = 0.8$ and

$\epsilon = 0.45$; a Newton iteration was used to home in on the precise location of the zeros of λ_B. In Fig.6, the three characteristic roots c of smallest absolute value lie on the real axis, located at $c \approx -0.375, 0.375$ and $c = 0$; these will be denoted by c_-, c_+ and c_0 respectively. The last of these, which is zero for all a, q and ϵ, corresponds to the exact solution of (28) and (29) $\bar{u} = \partial u_p/\partial x$ associated with an origin shift of u_p in x. Although Fig.6 shows two sets of roots in the first quadrant, the higher set can be ignored as it is just a reflection of the lower set about the line $c = iq$ and corresponds to the fact that any multiple of q in the imaginary part of c can also be incorporated in the periodic part of the Floquet form (30). The roots occur in conjugate pairs and also pairs symmetric about the imaginary axis, giving a quadruply-infinite set corresponding to the existence of a complete set of eigenfunctions in y, associated with the corresponding eigenvectors $\mathbf{f}$.

Calculations were extended to higher truncation levels N and $\bar{N}$, and also to other values of M. The results shown in Table 1 confirm that the severe truncation gives a good approximation to the position of the real eigenvalue; in fact the exponent is more sensitive to the discretization in y, as given by M, than the number of Fourier modes in either u_p or $\bar{u}$.

The roots $c_\pm$ are the most significant in terms of the spatial behaviour of the perturbation (30). Fig.7 shows their movement in the complex plane in the case $a = \pi$ and $\epsilon = 0.45$ for a range of wavenumbers q about the critical wavenumber $q_0 = 0.8223$. As the value of q is increased or decreased from q_0 a position is reached where $c_\pm$ become zero and thereafter become purely imaginary. This behaviour is shown for different values of ϵ in Fig.8. The wavenumbers at which $c_\pm = 0$ define the Eckhaus stability boundary (Eckhaus 1965) since these form the locus of points at which spatially oscillatory disturbances to the periodic solution u_p have zero temporal growth rate. Outside the Eckhaus boundary, spatially periodic solutions (25) are temporally unstable to periodic solutions of different wavelength.

Fig.9 shows the Eckhaus boundary computed with $M = 17$ for the case $a = \pi$, where $\epsilon_0 = 0.2206$. At low values of ϵ the zeros of $c_\pm$ depend sensitively on the value of M and, consistent with the trend shown in Table 1, the numerical computation overestimates the actual bandwidth. For values of ϵ near ϵ_0, the Eckhaus boundary can be calculated from the weakly nonlinear equation (19) by considering perturbations to A_0 in (22) of the form

$$\bar{A}(X) = \bar{K} e^{i\Omega X + CX}. \tag{34}$$

A non-trivial solution requires either $C = 0$ (associated with an origin shift of the periodic form) or $\alpha_1 C^2 + 6\alpha_1 \Omega^2 - 2\alpha_2 = 0$. Real values of C (corresponding to the non-existence of spatially periodic disturbances which grow with time) are confined to the region $\Omega^2 < \alpha_2/3\alpha_1$, equivalent to overall wavenumbers q in the range

$$q_0 - (\epsilon - \epsilon_0)^{1/2}(\alpha_2/3\alpha_1)^{1/2} < q < q_0 + (\epsilon - \epsilon_0)^{1/2}(\alpha_2/3\alpha_1)^{1/2} \tag{35}$$

as $\epsilon \to \epsilon_0$. This is also shown in Fig.9 for the case $a = \pi$.

4 Nonlinear solutions for a semi-infinite channel

If an end wall is placed across the channel at $x = 0$ to form a semi-infinite channel $x \geq 0$ then the band of stable wavenumbers is further restricted. We now calculate this restriction by numerical computation in the fully nonlinear regime and by asymptotic analysis in the weakly nonlinear regime.

4.1 Nonlinear solutions

Within the Eckhaus boundary where $c_+ > 0$, the results of section 3 indicate the existence of a (doubly-infinite) set of characteristic exponents c with $\mathrm{Re}(c) \geq 0$, corresponding to a complete set of eigenfunctions (30) which (for $\mathrm{Re}(c) > 0$) decay as $x \to \infty$. Satisfaction of the no-slip conditions (3) at the end wall requires a departure of the nonlinear solution from its periodic form (25) which is now achieved only as $x \to \infty$. From (27) and (30), the asymptotic form of the solution as $x \to \infty$ is expected to be

$$u \sim u_p(x + \phi, y) + ke^{-c_+ x} P(x + \phi, y). \tag{36}$$

Here ϕ is a possible constant phase shift of the solution which corresponds to the eigenvalue $c = 0$ and k is a real constant associated with the characteristic exponent c_+ and corresponding eigenfunction

$$P(x, y) = \sum_{n=0}^{\infty} \Big(b_n(y) \cos nqx + c_n(y) \sin nqx \Big). \tag{37}$$

The complete asymptotic form (36) will also contain components

$$k_m e^{-c_m x} P_m(x + \phi, y) + \text{c.c.}, \quad m = 1, 2 \ldots, \tag{38}$$

where k_m are (complex) constants associated with the remaining (complex) characteristic exponents c_m and corresponding eigenfunctions $P_m(x, y)$. In principle, the two real constants k and ϕ, together with the doubly-infinite set of real constants given by the real and imaginary parts of k_m must be chosen in order that the two end-wall conditions (3) are satisfied for all values of y. An approximate estimate of the restricted waveband can be made by assuming that (36) holds for all $x \geq 0$ and that u_p and the Floquet eigenfunction $P(x, y)$ are replaced by their one-mode approximations

$$u_p(x, y) = a_1(y) \sin qx, \quad P(x, y) = b_1(y) \cos qx + c_1(y) \sin qx. \tag{39}$$

Fig.10 shows the variation of a_1, b_1 and c_1 with wavenumber for the case where $a = \pi$ and $\epsilon = 0.4$. Noting that the profiles a_1, b_1 and c_1 are similar, it is a good approximation to apply (3) at the central point $y = 0$ only, equivalent to a one-point collocation. Elimination of k then leads to the requirement that the phase shift ϕ is determined by solutions of the equation

$$B_1 \sin 2q\phi - C_1 \cos 2q\phi = -2qc_+^{-1} B_1 - C_1, \tag{40}$$

where $B_1 = b_1(0)$ and $C_1 = c_1(0)$. The left-hand side is an oscillatory function of ϕ with amplitude $(B_1^2 + C_1^2)^{1/2}$ so that solutions exist only if

$$|2qc_+^{-1}B_1 + C_1| < (B_1^2 + C_1^2)^{1/2}. \tag{41}$$

For $\epsilon = 0.4$ and from the variation of c_+ shown in Fig.8 this is approximately the band of solutions shown in Fig.10. By extending the calculations to other values of ϵ, a narrow waveband of solutions is obtained in the q, ϵ plane and this is shown in Fig.9.

In order to calculate the waveband accurately the asymptotic solution (36) must be replaced by the actual steady-state solution of the nonlinear Swift-Hohenberg equation and the end wall conditions (3) must be applied at all values of y. This was achieved by using an explicit finite difference scheme to solve the time-dependent Swift-Hohenberg equation (1) in the domain $0 \le x \le x_\infty, -a \le y \le a$ subject to the no-slip conditions (2) and (3), and the periodicity condition

$$u = \frac{\partial^2 u}{\partial x^2} = 0 \text{ at } x = x_\infty. \tag{42}$$

A standard 13-point second-order accurate discretization of the spatial derivatives was used together with a forward difference in time. Steady-state solutions were found by allowing the solution to evolve from a specified initial state at $t = 0$, usually taken as $u = (a^2 - y^2)u_0 \sin(10\pi x/x_\infty)$ with $u_0 = 0.3/\pi^2$ for the case $a = \pi$. The value of x_∞ must be sufficiently large to accommodate the approach of the solution to its nonlinear periodic form and was generally set to the value $x_\infty = 10\pi/q_\infty$, with results then obtained for a series of values of q_∞ near the critical wavenumber q_0 for the infinite channel. The solution then converges to a steady (non-periodic) state and the actual wavelength λ, wavenumber $q = 2\pi/\lambda$ and amplitude can be deduced from the last half-cycle at $x = x_\infty$. The phase shift ϕ relative to the end wall can also be calculated since from (36) $x_\infty + \phi$ is an integer number of half wavelengths. Most results were obtained with a 100×20 grid and a time step $\Delta t = 2 \times 10^{-4}$; typically a steady-state solution was achieved for values of t in the range 300 to 800, depending on the values of ϵ, q and a. The scheme was tested by replacing the no-slip condition at $x = 0$ by a periodic condition, allowing nonlinear solutions for an infinite channel to be computed. This predicted a critical wavenumber $q_0 = 0.827$ at $\epsilon_0 = 0.222$ in the case $a = \pi$, consistent with the second-order accuracy of the scheme.

Fig.11 shows results for the phase shift ϕ as a function of q in the case $a = \pi$ and $\epsilon = 0.5$. Stable steady-state solutions are limited to the range $0.797 \le q \le 0.871$ with the end points corresponding to the positions where $dq/d\phi = 0$. This is similar to the behaviour in the one-dimensional case reported by Daniels et al (2003) where it was shown that dual solutions exist at internal points of the range, one of which is unstable. The same is expected in the two-dimensional case, but the method of solution adopted here precludes the determination of the unstable branch. Fig.12 shows contours of the steady-state solution for $a = \pi, \epsilon = 0.5$

and $q = 0.835$; also shown is the centre-line value $u(x,0)$ and the corresponding periodic form $u_p(x,0)$, illustrating the phase shift of the solution. Results for $a = \pi, \epsilon = 0.25$ and $q = 0.829$ are shown in Fig.13; as ϵ nears the critical value $\epsilon_0 = 0.22$ the approach of the solution to its nonlinear periodic form occurs over an increasingly long length scale in x.

By repeating the calculations for a range of values of ϵ, the restricted band of wavenumbers is determined and is shown in Fig.9 for the case $a = \pi$. The bandwidth is similar to that predicted by the Floquet approximation, but is more centrally placed relative to the critical wavenumber.

4.2 Weakly nonlinear analysis $\epsilon - \epsilon_0 \ll 1$

More insight into the role of the channel halfwidth a can be gained by extending the weakly nonlinear theory of section 2.2 to provide a prediction of the restricted waveband for values of ϵ close to ϵ_0. This requires a derivation of the equation for the second amplitude function A_1 which appears in the solution (17) for u_1. This is found by consideration of the solvability condition for the term u_3 in (12), which satisfies

$$\mathcal{L}u_3 = -2\left(1+\frac{\partial^2}{\partial x^2}+\frac{\partial^2}{\partial y^2}\right)\left(2\frac{\partial^2 u_2}{\partial x \partial X}+\frac{\partial^2 u_1}{\partial X^2}\right)-4\frac{\partial^4 u_1}{\partial x^2 \partial X^2}-4\frac{\partial^4 u_0}{\partial x \partial X^3}+u_1-3u_0^2 u_1. \tag{43}$$

It is shown in Appendix B that this leads to the amplitude equation

$$\alpha_1 A_1'' + \alpha_2 A_1 - \alpha_3(A_0^2 A_1^* + 2A_0 A_0^* A_1) = i(\alpha_4 A_0''' + \alpha_5 A_0' + \alpha_6 A_0^2 A_0'^* + \alpha_7 A_0 A_0^* A_0'), \tag{44}$$

where the coefficients $\alpha_i (i = 4,5,6,7)$ are real and given by

$$\alpha_4 = a^3 q_0^3 \alpha_{40} + a q_0 \alpha_{41}, \quad \alpha_5 = a^3 q_0 \alpha_{50}, \quad \alpha_6 = -\alpha_7/2 = a^3 q_0 \alpha_{60}, \tag{45}$$

where

$$\alpha_{40} = 0.06516, \quad \alpha_{41} = 2.926, \quad \alpha_{50} = 0.01323, \quad \alpha_{60} = 0.01132. \tag{46}$$

The four terms on the right-hand side of (44) are actually linearly dependent because the first term A_0''' can be expressed in terms of the other three using (19).

The expansion (12) is valid over the long length scale $x \sim \epsilon^{-1/2}$ and this outer solution must be matched with an inner solution close to the end wall where $x \sim 1$ and there is an adjustment to the end-wall conditions (3). In this inner region the solution can be expanded in the form

$$u = \bar{\epsilon} U(x,y) + \ldots, \quad \bar{\epsilon} \to 0 \tag{47}$$

and is smaller, by a factor of $\bar{\epsilon}^{1/2}$, than that in the outer region. This is a consequence of the need to satisfy (3) and of consistency in matching between the

regions, to be discussed below. Substitution in (1) shows that U satisfies the partial differential equation

$$\mathcal{L}U = \left(\left(1 + \frac{\partial^2}{\partial x^2} + \frac{\partial^2}{\partial y^2}\right)^2 - \epsilon_0\right)U = 0. \tag{48}$$

This has general solution satisfying the boundary conditions $U = \partial U/\partial y = 0$ at $y = \pm a$ given by

$$U = \left\{(r_0 f_0(y) + s(x f_0(y) - i g_0(y)))e^{iq_0 x} + \sum_{n=1}^{\infty} r_n f_n(y) e^{iq_n x}\right\} + \text{c.c.}, \tag{49}$$

where $r_n, n = 0, 1, \ldots$ and s are arbitrary complex constants, f_0 and g_0 are the real functions defined in section 2 and f_n and $q_n, n = 1, 2, \ldots$ are the complex eigenfunctions and eigenvalues of the system

$$f_n'''' + 2(1 - q_n^2)f_n'' + ((1 - q_n^2)^2 - \epsilon_0)f_n = 0; \quad f_n = f_n' = 0 \quad (y = \pm a) \tag{50}$$

such that $\mathrm{Im}(q_n) > 0$. Solutions for which $\mathrm{Im}(q_n) < 0$ are discarded since these would grow exponentially as $x \to \infty$, whilst the solution for $n = 0$ with zero imaginary part corresponds to the critical wavenumber q_0. It is convenient to set

$$r_{nr,i} = \chi_{nr,i} s_r + \bar{\chi}_{nr,i} s_i \tag{51}$$

where $r_{nr,i}$ and $s_{r,i}$ denote the real and imaginary parts of r_n and s, and it is shown in Appendix C that the coefficients $\chi_{nr,i}$ and $\bar{\chi}_{nr,i}$ are then determined as functions of a from (49) by application of the boundary conditions $U = \partial U/\partial x = 0$ at $x = 0$. Values of $\chi_{nr,i}$ and $\bar{\chi}_{nr,i}$ for $a = \pi$ are shown in Table 2.

Matching between the inner solution (47) as $x \to \infty$ and the outer solution (12) as $X \to 0$ requires that

$$A_0(0) = 0. \tag{52}$$

This is because if A_0 is non-zero at $X = 0$ an inner solution for u of order $\bar{\epsilon}^{1/2}$ would be generated similar in form to (49) but with the terms linear in x excluded; the remaining coefficients r_n could not then be chosen to satisfy both of the end-wall conditions at $x = 0$. Matching also requires $r_0 = A_1(0)$ and $s = A_0'(0)$ from which it follows, by setting $n = 0$ in (51), that

$$A_1(0) = \alpha A_0'(0) + \beta A_0'^*(0), \tag{53}$$

where

$$\alpha = (\chi_{0r} + \bar{\chi}_{0i} + i(\chi_{0i} - \bar{\chi}_{0r}))/2, \tag{54}$$

$$\beta = (\chi_{0r} - \bar{\chi}_{0i} + i(\chi_{0i} + \bar{\chi}_{0r}))/2. \tag{55}$$

Values of α and β for various values of a are given in Table 3.

The results (52) and (53) are boundary conditions at $X = 0$ for the amplitude functions A_0 and A_1 in the outer region, allowing A_0 to be determined as

$$A_0 = \left(\frac{\alpha_2}{\alpha_3}\right)^{1/2} e^{i\psi} \tanh \frac{\bar{X}}{\sqrt{2}} \tag{56}$$

where ψ is an arbitrary constant phase and then A_1 as

$$A_1 = \frac{\alpha_2}{(\alpha_1\alpha_3)^{1/2}} e^{i\psi} \Big\{ \bar{a} \operatorname{sech}^2 \frac{\bar{X}}{\sqrt{2}} + i \Big(\bar{b} \tanh \frac{\bar{X}}{\sqrt{2}} + \bar{q} \Big(\bar{X} \tanh \frac{\bar{X}}{\sqrt{2}} - \sqrt{2} \Big) + \frac{l_1}{\sqrt{2}} + \frac{(l_2 + l_3)}{2\sqrt{2}} \operatorname{sech}^2 \frac{\bar{X}}{\sqrt{2}} \Big) \Big\}, \tag{57}$$

where $\bar{X} = (\alpha_2/\alpha_1)^{1/2} X$,

$$\bar{a} = (\alpha_r + |\beta| \cos(\gamma - 2\psi))/\sqrt{2}, \tag{58}$$

$$\bar{q} = (2l_1 + l_2 + l_3 - 2\alpha_i - 2|\beta| \sin(\gamma - 2\psi))/4, \tag{59}$$

$$l_1 = \frac{\alpha_5}{\alpha_2} - \frac{\alpha_4}{\alpha_1}, \quad l_2 = \frac{\alpha_4}{\alpha_1} + \frac{\alpha_6}{\alpha_3}, \quad l_3 = 2\left(\frac{\alpha_4}{\alpha_1} - \frac{\alpha_6}{\alpha_3}\right), \tag{60}$$

$\alpha_{r,i}$ are the real and imaginary parts of α, and $\beta = |\beta| e^{i\gamma}$. The constant $\bar{b}$ remains arbitrary at this stage of the expansion in $\bar{\epsilon}$.

From (56) and (57), as $X \to \infty$,

$$u \sim \bar{\epsilon}^{1/2} (\alpha_2/\alpha_3)^{1/2} f_0(y) e^{i\psi + iq_0 x} \{1 + i\bar{\epsilon}^{1/2} \alpha_2 \alpha_1^{-1} \bar{q} X + \ldots\} + \text{c.c.} \tag{61}$$

and the solution assumes the form

$$u \sim \bar{\epsilon}^{1/2} (\alpha_2/\alpha_3)^{1/2} f_0(y) \exp\{i(q_0 + \bar{\epsilon}\alpha_2\alpha_1^{-1}\bar{q})x + i\psi\} + \text{c.c.} \tag{62}$$

equivalent to that in an infinite channel with wavenumber

$$q_0 + \bar{\epsilon}\alpha_2\alpha_1^{-1}\bar{q}. \tag{63}$$

This can be formally confirmed by carrying out a weakly nonlinear expansion with dual length scales $x \sim 1$ and $x \sim \bar{\epsilon}^{-1}$ but the details are similar to those already outlined in section 2 and in the one-dimensional case (Cross et al 1983) and are omitted here. The results (63) and (59) now show that as the phase ψ varies, the permissable values of the wavenumber q are limited to the range

$$q_0 + (\epsilon - \epsilon_0)(\theta - \frac{w}{2}) < q < q_0 + (\epsilon - \epsilon_0)(\theta + \frac{w}{2}) \tag{64}$$

as $\epsilon \to \epsilon_0$, where

$$w = \alpha_2|\beta|/\alpha_1, \quad \theta = \alpha_2(2l_1 + l_2 + l_3 - 2\alpha_i)/(4\alpha_1). \tag{65}$$

This represents a region in the q, ϵ plane that expands linearly from the critical point (q_0, ϵ_0). The width $\bar{\epsilon}w$ and angle $\bar{\epsilon}\theta$ of this linear segment depend on the channel halfwidth a in the manner shown in Fig.14, and Fig.15 shows the waveband in the q, ϵ plane for several different values of a. The results for $a = \pi$ are also included in Fig.9 and are seen to agree well with the fully nonlinear calculations of section 4.1.

It is seen from Fig.14 that the waveband is generally asymmetric, being skewed towards subcritical wavenumbers for $a < 2.567$ and supercritical wavenumbers for $a > 2.567$. For $a > 7.15$, the entire waveband is restricted to supercritical wavenumbers and it is interesting to compare this with the corresponding result for the one-dimensional (that is, y-independent) problem (Cross et al 1983) where solutions for a semi-infinite domain $x \geq 0$ are restricted to the symmetric range

$$1 - \frac{\epsilon}{16} < q < 1 + \frac{\epsilon}{16}, \quad \epsilon \ll 1 \tag{66}$$

either side of the critical wavenumber $q_0 = 1$. The explanation of this apparent contradiction is that the large a limit of the present analysis cannot be compared directly with (66). As $a \to \infty$, the expansion (12) is effectively limited to the range $\bar{\epsilon}a^4 \ll 1$, equivalent to $\epsilon - \epsilon_0 \ll a^{-4}$. In this range the solution varies with y in the region $-a \leq y \leq a$ (through the functions $f_0(y)$ and so on). As nonlinear effects increase, a transition occurs over the range $\epsilon \sim a^{-4}$ in which the y-dependence of the solution is relegated to the neighbourhood of the channel walls. The one-dimensional solution then applies throughout most of the channel for $a^{-4} \ll \epsilon \ll 1$ with the wavenumber restriction (66) then applicable. The reason that the waveband (64) is skewed towards supercritical wavenumbers for large a can now be understood: from (11), the critical wavenumber has the form $q_0 \sim 1 - 1.598a^{-2}$ as $a \to \infty$ which means that the wavenumber must *increase* as ϵ increases through the range where $\epsilon - \epsilon_0 \sim a^{-4}$ and $q - q_0 \sim a^{-2}$ in order that the symmetric form (66) is attained when $a^{-4} \ll \epsilon \ll 1$. The transition from (64) to (66) is a problem of some interest, especially as a further feature is the onset of rolls perpendicular to the end wall when ϵ reaches values of order a^{-2}.

As the channel width decreases to $a = 1.788$ the critical wavelength becomes infinite. Although this behaviour is not relevant in the classical Rayleigh-Benard system, it is of interest in relation to convection between poorly conducting planes (Proctor 1981). Fig.14 shows that in this limit the bandwidth increases and the long wavelength solutions include both subcritical and supercritical modes.

For a pattern of wavenumber q in the range (64), equation (59) determines the corresponding phase shift ψ. In fact it determines two solution branches for a given wavenumber, corresponding to $\psi = \psi_0$ (say) and $\psi = \gamma - \frac{\pi}{2} - \psi_0$. Since, from (56), $A_0'(0) = s = \alpha_2^{1/2} e^{i\psi}/(2\alpha_3)^{1/2}$, these two branches are associated with

$$s_{r,i} = \alpha_2^{1/2}(2\alpha_3)^{-1/2}(\cos\psi_0, \sin\psi_0) \tag{67}$$

and

$$s_{r,i} = \alpha_2^{1/2}(2\alpha_3)^{-1/2}(\sin(\gamma - \psi_0), -\cos(\gamma - \psi_0)) \tag{68}$$

respectively. The inner solution near the end wall is then determined by (49) as a function of the phase shift ψ_0, which varies over the range $\frac{1}{2}\gamma - \frac{\pi}{4} < \psi_0 < \frac{1}{2}\gamma + \frac{\pi}{4}$ as q varies over the range (64). Fig.16 shows contours of the inner solution U corresponding to the two branches (67) and (68) at the midpoint of the range, $\psi_0 = \frac{1}{2}\gamma$, for the case $a = \pi$. Branch (67) is a stable solution and compares well with the nonlinear computation in Fig.13 whereas branch (68) involves a flow reversal close to the end wall and is an unstable solution.

5 Discussion

Nonlinear steady-state solutions of the two-dimensional Swift-Hohenberg equation have been found for an infinite channel of non–dimensional width $2a$. Floquet theory has been used to investigate the departure of the solution from its periodic form, leading to the determination of the Eckhaus stability boundary and the asymptotic form of the solution at large distances from an end wall inserted across the channel. The phase shift of this asymptotic form has been found as a function of wavelength by numerical computation in the fully nonlinear case and by weakly nonlinear theory for values of ϵ close to the threshold value ϵ_0, leading to the determination of the restricted band of wavelengths possible in a semi-infinite channel.

If a second end wall is present then the waveband is quantized. Using the same procedure as that described for the one-dimensional case by Daniels et al (2003), the present results then also determine the families of steady-state solutions even or odd in x (together with their interconnecting branches) that exist in long finite channels.

One advantage of the weakly nonlinear treatment of section 4.2 is that the dependence on the channel halfwidth a can be incorporated analytically throughout most of the theory. This leads to the interesting result shown in Fig.14 that the waveband is skewed towards supercritical wavenumbers for sufficiently wide channels. Since the critical wavenumber for Rayleigh-Benard convection in a rigid, thermally conducting channel (Chana & Daniels 1989) has a qualitatively similar behaviour at large a to that of the Swift-Hohenberg system in (11) it is expected that the same behaviour will occur there.

It is now planned to apply the techniques and insight developed here in two dimensions to the three-dimensional convection problem. Rayleigh-Benard experiments in long boxes have identified significantly different and as yet unexplained behaviours for high and low Prandtl number fluids. At high Prandtl numbers little change in wavelength is observed as the Rayleigh number increases to as much as ten times its critical value whereas at low Prandtl numbers the wavelength is observed to increase steadily through the same range (Kirchartz & Oertel 1988). It is hoped that the present approach will provide new insight into this behaviour and also a way of predicting the behaviour of other similar pattern-forming systems.

Acknowledgment
This work was partly supported by a research grant from the EPSRC Applied Nonlinear Mathematics Programme.

References

Arter, W. & Newell, A.C. 1988 Numerical simulation of Rayleigh-Benard convection in shallow tanks, *Phys.Fluids*, **31**, 474-2485.

Chana, M.S. & Daniels, P.G. 1989 Onset of Rayleigh-Benard convection in a rigid channel, *J.Fluid Mech.* **199**, 257-279.

Cross, M.C., Daniels, P.G., Hohenberg, P.C. & Siggia, E.D. 1983 Phase-winding solutions in a finite container above the convective threshold, *J.Fluid Mech.* **127**, 155-183.

Cross, M.C. & Hohenberg, P.C. 1993 Pattern formation outside of equilibrium, *Rev.Mod.Phys.* **65**, 851-1112.

Daniels, P.G. & Chana, M.S. 1987 Multiple convective states in a long box heated from below, *Proc. ASME Winter Annual Meeting, Boston* HTD **94**, 49-57.

Daniels, P.G., Ho, D. & Skeldon, A.C. 2003 Solutions for nonlinear convection in the presence of a lateral boundary, *Physica* D**178**, 83-102.

Daniels, P.G. & Ong, C.F. 1990 Nonlinear convection in a rigid channel uniformly heated from below, *J.Fluid Mech.* **215**, 503-523.

Davies-Jones, R.P. 1970 Thermal convection in an infinite channel with no-slip sidewalls, *J.Fluid Mech.* **44**, 695-704.

Eckhaus, V. 1965 *Studies in Nonlinear Stability Theory.* Springer Tracts in Natural Philosophy, vol.6, Springer.

Kirchartz, K.R. & Oertel, H. 1988 Three-dimensional thermal cellular convection in rectangular boxes, *J.Fluid Mech.* **192**, 249-286.

Kramer, L. & Hohenberg, P.C. 1984 Effects of boundary conditions on spatially periodic states, *Physica* D**13**, 357-369.

Luijkx, J.M. & Platten, J.K. 1981 On the onset of free convection in a rectangular channel, *J.Non-Equil.Thermodyn.* **6**, 141-158.

Proctor, M.R.E. 1981 Planform selection by finite-amplitude thermal convection between poorly conducting slabs, *J.Fluid Mech.* **113**, 469-485.

Swift, J. & Hohenberg, P.C. 1977 Hydrodynamic fluctuation at the convective instability, *Phys.Rev.* A**15**, 319-328.

Appendix A. Derivation of the amplitude equation for A_0

From (8),

$$F_0(Y) = \frac{\cos\bar{\mu}_0\cosh\mu_0 Y - \cosh\mu_0\cos\bar{\mu}_0 Y}{\cos\bar{\mu}_0 - \cosh\mu_0} = 0.3422\cosh\mu_0 Y + 0.6578\cos\bar{\mu}_0 Y \tag{69}$$

and then $g_0 = a^2 q_0 G_0(Y)$ where

$$LG_0 \equiv G_0'''' + 2Q_0 G_0'' + (Q_0^2 - \delta_0)G_0 = 4(F_0'' + Q_0 F_0); \quad G_0 = G_0' = 0 \quad (Y = \pm 1) \tag{70}$$

with $G_0(0) = 0$ to fix the otherwise arbitrary multiple of the complementary solution F_0; the same solution can also be calculated from (7) as $G_0 = -2\partial F/\partial Q|_{\delta_0}$, giving

$$\begin{aligned} G_0 &= \frac{Y}{\nu_0 + \bar{\nu}_0}\left(\frac{\nu_0}{\mu_0}\sinh\mu_0 Y + \frac{\bar{\nu}_0}{\bar{\mu}_0}\sin\bar{\mu}_0 Y\right) - \frac{2\nu_0\bar{\nu}_0\delta_0^{1/2}(\cosh\mu_0 Y - \cos\bar{\mu}_0 Y)}{(\delta_0 - Q_0^2)(\nu_0 + \bar{\nu}_0)^2} \\ &= Y(0.2852\sinh\mu_0 Y + 0.2350\sin\bar{\mu}_0 Y) - 0.1851(\cosh\mu_0 Y - \cos\bar{\mu}_0 Y) \end{aligned} \tag{71}$$

where

$$\nu_0 = (\delta_0 - \delta_0^{1/2} - Q_0^2 - Q_0)^{1/2}, \;\; \bar{\nu}_0 = (\delta_0 + \delta_0^{1/2} - Q_0^2 - Q_0)^{1/2}. \tag{72}$$

The functions F_0 and G_0 are shown in Fig.17.

The function h in (18) satisfies

$$\bar{\mathcal{L}}h \equiv \left(\left(1 - q_0^2 + \frac{\partial^2}{\partial y^2}\right)^2 - \epsilon_0\right)h = \xi(y, X); \quad h = \frac{\partial h}{\partial y} = 0 \quad (y = \pm a), \tag{73}$$

where

$$\xi = A_0 f_0 - 3A_0^2 A_0^* f_0^3 - A_0''\left(4q_0\left(1 - q_0^2 + \frac{d^2}{dy^2}\right)g_0 + 2\left(1 - 3q_0^2 + \frac{d^2}{dy^2}\right)f_0\right). \tag{74}$$

The linear homogeneous system (5) is self-adjoint and since the inhomogeneous system for h involves the same linear operator it has a consistent solution only if

$$\int_{-a}^{a} \xi f_0 dy = 0. \tag{75}$$

This gives (19) and (20) where

$$\alpha_{10} = -4\int_{-1}^{1} F_0(G_0'' + Q_0 G_0 - F_0)dY, \tag{76}$$

$$\alpha_{11} = -2\int_{-1}^{1} F_0(F_0'' + Q_0 F_0)dY, \tag{77}$$

$$\alpha_{20} = \int_{-1}^{1} F_0^2 dY, \tag{78}$$

$$\alpha_{30} = 3\int_{-1}^{1} F_0^4 dY \tag{79}$$

and evaluation of the integrals using (69) and (71) gives (21).

Appendix B. Derivation of the amplitude equation for A_1

It is first necessary to complete the solution for u_2 in (18). By expressing the nonlinear term $A_0^2 A_0^*$ on the right-hand side of (74) in terms of A_0'' and A_0 from (19), the solution for the function h can be found in the form

$$h = A_0''\{a^4 q_0^2 H_1(Y) + a^2 H_2(Y)\} + A_0 a^4 H_3(Y), \tag{80}$$

where $H_{1,2,3}$ satisfy

$$LH_1 = -4(G_0'' + Q_0 G_0 - F_0) - 3\alpha_{10}\alpha_{30}^{-1} F_0^3; \quad H_1 = H_1' = 0 \quad (Y = \pm 1), \tag{81}$$

$$LH_2 = -2(F_0'' + Q_0 F_0) - 3\alpha_{11}\alpha_{30}^{-1} F_0^3; \quad H_2 = H_2' = 0 \quad (Y = \pm 1), \tag{82}$$

$$LH_3 = F_0 - 3\alpha_{20}\alpha_{30}^{-1} F_0^3; \quad H_3 = H_3' = 0 \quad (Y = \pm 1). \tag{83}$$

Since $\alpha_{11} = 0$, equations (70) and (82) differ by a factor of minus two on the right-hand side and hence the solution for H_2 can be taken as $H_2 = -G_0/2$. Since F_0 and G_0 are known, the remaining equations (81) and (83) can also be solved analytically. Maple was used to aid with the algebra, giving

$$\begin{aligned} H_1 = {} & (d_1 + d_2 Y^2)\cosh(\mu_0 Y) + (d_3 + d_4 Y^2)\cos(\bar{\mu}_0 Y) \\ & + Y(d_5 \sinh(\mu_0 Y) + d_6 \sin(\bar{\mu}_0 Y)) + d_7 \cosh(3\mu_0 Y) + d_8 \cos(3\bar{\mu}_0 Y) \\ & + d_9 \cos(\bar{\mu}_0 Y)\cosh(2\mu_0 Y) + d_{10}\sin(\bar{\mu}_0 Y)\sinh(2\mu_0 Y) \\ & + d_{11}\cos(2\bar{\mu}_0 Y)\cosh(\mu_0 Y) + d_{12}\sin(2\bar{\mu}_0 Y)\sinh(\mu_0 Y), \end{aligned} \tag{84}$$

$$\begin{aligned} H_3 = {} & d_{13}\cosh(\mu_0 Y) + d_{14}\cos(\bar{\mu}_0 Y) \\ & + Y(d_{15}\sinh(\mu_0 Y) + d_{16}\sin(\bar{\mu}_0 Y)) + d_{17}\cosh(3\mu_0 Y) + d_{18}\cos(3\bar{\mu}_0 Y) \\ & + d_{19}\cos(\bar{\mu}_0 Y)\cosh(2\mu_0 Y) + d_{20}\sin(\bar{\mu}_0 Y)\sinh(2\mu_0 Y) \\ & + d_{21}\cos(2\bar{\mu}_0 Y)\cosh(\mu_0 Y) + d_{22}\sin(2\bar{\mu}_0 Y)\sinh(\mu_0 Y). \end{aligned} \tag{85}$$

Here the coefficients d_1 to d_{22} are functions of Q_0 and δ_0 given to four significant figures by

$$\begin{aligned} & d_1 = -0.0006539, d_2 = -0.1189, d_3 = -0.001294, d_4 = -0.04200 \\ & d_5 = 0.1943, d_6 = -0.04810, d_7 = -0.0002183, d_8 = -0.00008236, \\ & d_9 = 0.002938, d_{10} = -0.0004413, d_{11} = -0.0007635, d_{12} = 0.001072, \\ & d_{13} = 0.002506, d_{14} = -0.002998, d_{15} = -0.0001211, d_{16} = -0.004005 \\ & d_{17} = -0.00005726, d_{18} = -0.00002160, d_{19} = 0.0007706, d_{20} = -0.0001158 \\ & d_{21} = -0.0002003, d_{22} = 0.002812. \end{aligned} \tag{86}$$

The normalization conditions $H_1(0) = 0$ and $H_3(0) = 0$ have been applied to completely determine all the coefficients. The functions H_1 and H_3 are shown in Fig.17.

The remaining function involved in the solution (18) for u_2 is h_0 which satisfies

$$\left(1 - 9q_0^2 + \frac{d^2}{dy^2}\right)^2 h_0 - \epsilon_0 h_0 = -f_0^3; \quad h_0 = h_0' = 0 \quad (y = \pm a). \tag{87}$$

Since this involves a different linear operator it is not possible to scale out the channel halfwidth a, but the function h_0 is not needed to calculate the coefficients $\alpha_4, \ldots, \alpha_7$. These now follow from the solvability condition associated with terms proportional to $e^{\pm iq_0 x}$ in (43), giving the results (44) and (45) where

$$\alpha_{40} = 4\int_{-1}^{1} F_0(H_1'' + Q_0 H_1 + G_0)dY, \tag{88}$$

$$\alpha_{41} = 2\int_{-1}^{1} F_0(2H_2'' + 2Q_0 H_2 + 2F_0 - G_0'' - Q_0 G_0)dY, \tag{89}$$

$$\alpha_{50} = \int_{-1}^{1} F_0(4H_3'' + 4Q_0 H_3 + G_0)dY, \tag{90}$$

$$\alpha_{60} = 3\int_{-1}^{1} F_0^3 G_0 dY. \tag{91}$$

Evaluation of these integrals using Maple gives the results (46).

Appendix C. Derivation of the coefficients χ and $\bar{\chi}$

The channel halfwidth a is removed from the system (50) by the transformations $f_n(y) = F_n(Y), q_n^2 = 1 - Q_n a^{-2}$, giving

$$F_n'''' + 2Q_n F_n'' + (Q_n^2 - \delta_0)F_n = 0; \quad F_n = F_n' = 0 \quad (Y = \pm 1). \tag{92}$$

This has solutions that are either even or odd in Y but for the present purposes it is sufficient to determine the even set. With a normalization $F_n(0) = 1$, this is given by

$$F_n = \frac{\cos\bar{\mu}_n \cosh\mu_n Y - \cosh\mu_n \cos\bar{\mu}_n Y}{\cos\bar{\mu}_n - \cosh\mu_n} \tag{93}$$

where

$$\mu_n = (\delta_0^{1/2} - Q_n)^{1/2}, \quad \bar{\mu}_n = (\delta_0^{1/2} + Q_n)^{1/2} \tag{94}$$

are generally complex. Insisting that (93) satisfies the boundary conditions requires that

$$\bar{\mu}_n \cosh\mu_n \sin\bar{\mu}_n + \mu_n \cos\bar{\mu}_n \sinh\mu_n = 0. \tag{95}$$

Splitting (95) into real and imaginary parts gives two sets of real equations for the real and imaginary parts $\mu_{nr,i}$ and $\bar{\mu}_{nr,i}$ of μ_n and $\bar{\mu}_n$ respectively. However,

these are also related by (94) and taking the real and imaginary parts gives two further sets of equations

$$\bar{\mu}_{nr} = -\mu_{nr}\mu_{ni}/\bar{\mu}_{ni} \tag{96}$$

and

$$\bar{\mu}_{ni}^2 = \frac{1}{2}\left\{\mu_{nr}^2 - \mu_{ni}^2 - 2\delta_0^{1/2} + \left((\mu_{nr}^2 - \mu_{ni}^2 - 2\delta_0^{1/2})^2 + 4\mu_{nr}^2\mu_{ni}^2\right)^{1/2}\right\}. \tag{97}$$

These were used to express $\bar{\mu}_{nr,i}$ in terms of $\mu_{nr,i}$ and then Newton's method used to solve the two remaining sets of equations for $\mu_{nr,i}$. The real and imaginary parts of Q_n are then calculated from (94) as

$$Q_{nr} = \mu_{ni}^2 - \mu_{nr}^2 + \delta_0^{1/2}, \quad Q_{ni} = -2\mu_{nr}\mu_{ni}, \tag{98}$$

respectively. It is sufficient to find solutions in one quadrant of the μ_{nr}, μ_{ni} plane because the system (95)-(97) is invariant under the transformation $\mu_{nr} \to -\mu_{nr}$ and also under $\mu_{ni} \to -\mu_{ni}$. Each solution for $\mu_{nr,i}$ in the positive quadrant therefore yields four solutions in the complex plane. In turn these four solutions provide the eigenvalue Q_n and its complex conjugate for each value of n. The solution that lies on the axis $\mu_{ni} = 0$ gives the critical wavenumber $Q_0 = 3.196$. The six complex eigenvalues with (in magnitude) smallest non-zero imaginary part are listed in Table 4 and the corresponding eigenfunctions are shown in Fig.18.

Introducing (51), the solution (49) satisfies the end-wall conditions $U = \partial U/\partial x = 0$ if the coefficients χ_n satisfy

$$\chi_{0r}F_0 + \sum_{n=1}^{\infty}(\chi_{nr}F_{nr} - \chi_{ni}F_{ni}) = 0, \tag{99}$$

$$q_0\chi_{0i}F_0 + \sum_{n=1}^{\infty}(q_{ni}\chi_{nr} + q_{nr}\chi_{ni})F_{nr} + \sum_{n=1}^{\infty}(q_{nr}\chi_{nr} - q_{ni}\chi_{ni})F_{ni} = F_0 + a^2q_0^2G_0 \tag{100}$$

and the coefficients $\bar{\chi}_n$ satisfy

$$\bar{\chi}_{0r}F_0 + \sum_{n=1}^{\infty}(\bar{\chi}_{nr}F_{nr} - \bar{\chi}_{ni}F_{ni}) = -a^2q_0G_0, \tag{101}$$

$$q_0\bar{\chi}_{0i}F_0 + \sum_{n=1}^{\infty}(q_{ni}\bar{\chi}_{nr} + q_{nr}\bar{\chi}_{ni})F_{nr} + \sum_{n=1}^{\infty}(q_{nr}\bar{\chi}_{nr} - q_{ni}\bar{\chi}_{ni})F_{ni} = 0. \tag{102}$$

Truncated forms of these equations were solved by a collocation method, evaluating each pair at $Y = 0$ together with $\bar{M}$ equally-spaced locations in the interval $0 < Y < 1$, yielding $2(\bar{M}+1)$ equations for the $2(\bar{M}+1)$ coefficients $\chi_{nr,i}$ or $\bar{\chi}_{nr,i}, n = 0, 1 \ldots \bar{M}$. Good convergence was achieved as the value of $\bar{M}$ was increased - the results given in Table 2 are for $\bar{M} = 6$.

M	N	$\bar{N}$	c_+
8	1	1	0.3988
17	1	1	0.3750
35	1	1	0.3697
71	1	1	0.3685
17	3	1	0.3749
17	3	3	0.3752

Table 1. Value of the critical exponent c_+ for $a = \pi, \epsilon = 0.45$ and $q = 0.8$ for different values of M, N and $\bar{N}$.

n	χ_{nr}	χ_{ni}	$\bar{\chi}_{nr}$	$\bar{\chi}_{ni}$
0	-0.02201	1.29750	-0.15395	-0.07450
1	0.00163	-0.20391	0.14752	-0.31646
2	0.02468	-0.00649	0.01132	0.04062
3	-0.00520	0.00722	-0.00705	-0.00615
4	0.00090	-0.00384	0.00311	0.00041
5	0.00032	0.00188	-0.00116	0.00086
6	-0.00033	-0.00024	0.00021	-0.00045

Table 2. Values of $\chi_{nr,i}$ and $\bar{\chi}_{nr,i}$ for $a = \pi$.

a	α	β
2.00	-0.03259+1.14116i	0.03068+1.10493i
3.14	-0.04825+0.72573i	0.02625+0.57177i
4.00	-0.05787+0.76647i	0.01177+0.51181i
6.00	-0.08204+1.02209i	-0.01498+0.48789i
8.00	-0.13021+1.41751i	-0.01811+0.48421i
10.00	-0.19755+1.93484i	-0.01994+0.48268i

Table 3. Values of α and β for various values of a.

n	Q_n	n	Q_n
1	26.30-15.86i	4	216.45-60.56i
2	69.73-29.87i	5	319.59-76.93i
3	133.15-44.83i	6	442.53-93.82i

Table 4. Eigenvalues Q_n listed in order of descending imaginary part.

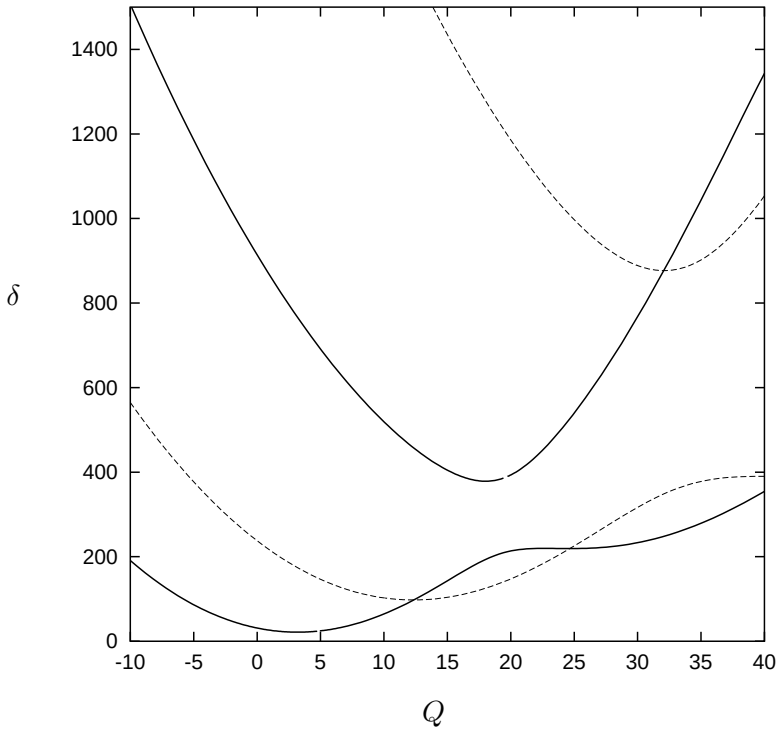

Figure 1: Marginal stability curves in the Q, δ plane showing the two lowest even branches (—) and the two lowest odd branches (- - -).

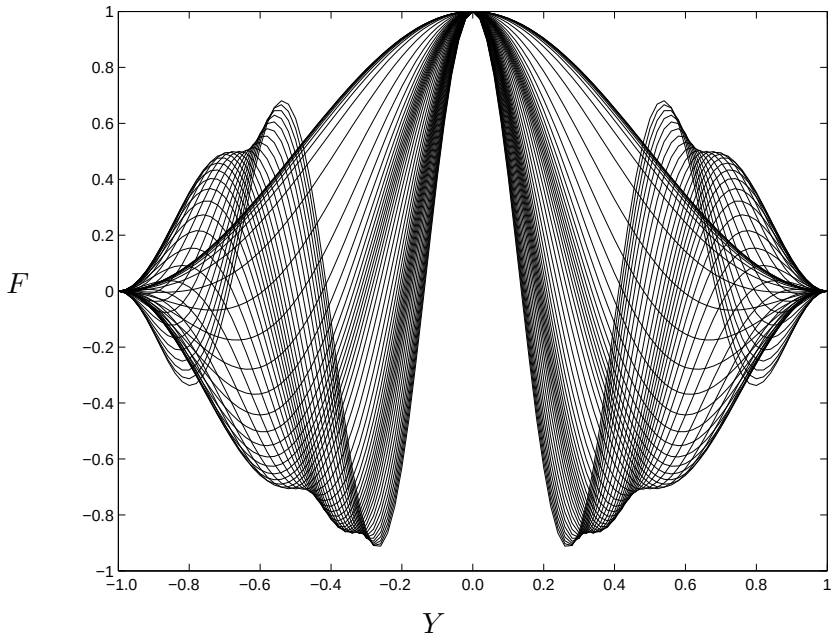

Figure 2: Variation of the profile $F(Y)$ for values of Q increasing from Q_0 on the lowest even marginal stability curve.

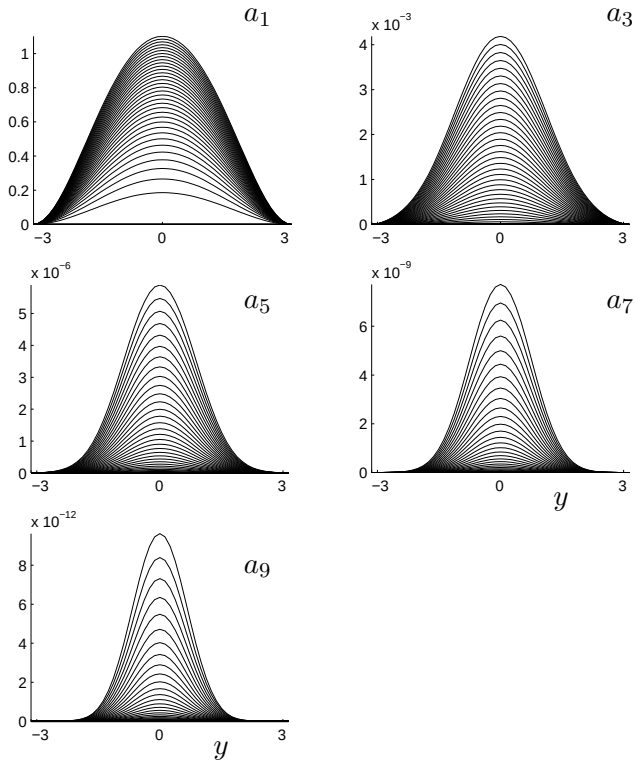

Figure 3: Fourier coefficients $a_n(y)$ of the nonlinear periodic solution for $n = 1, 3, 5, 7, 9$ as a function of y for $a = \pi, q = 1$ and values of ϵ decreasing from 1 in steps of 0.02.

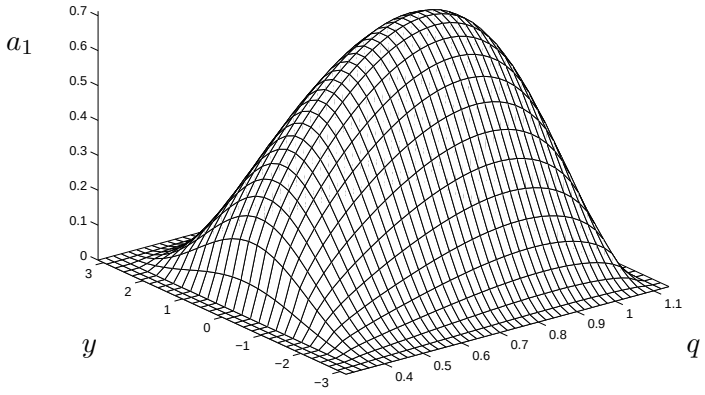

Figure 4: Fourier coefficient $a_1(y)$ of the nonlinear periodic solution as a function of y and q for $a = \pi$ and $\epsilon = 0.5$.

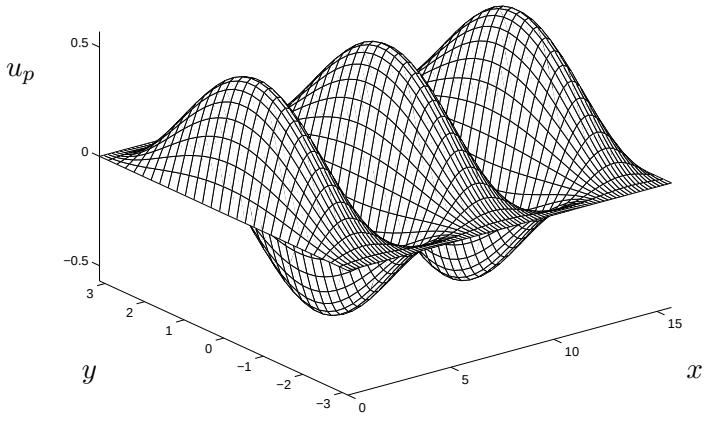

Figure 5: Periodic solution $u_p(x, y)$ as a function of x and y for $a = \pi, q = 1$ and $\epsilon = 0.5$.

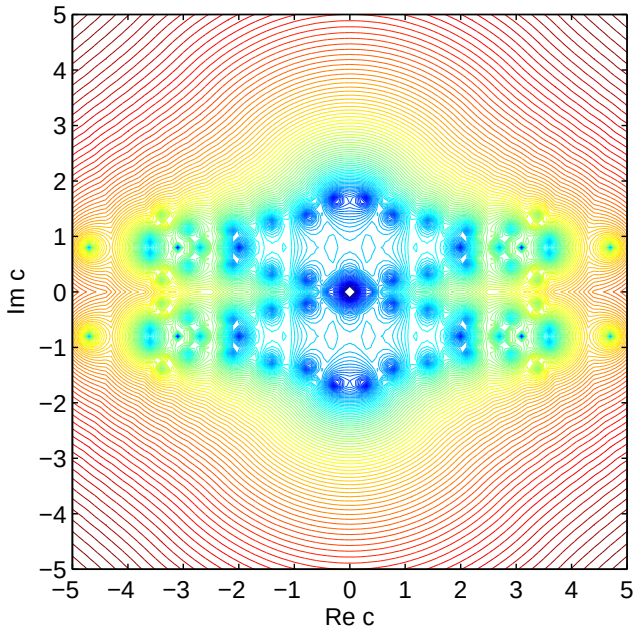

Figure 6: Contour plot of $\log \lambda_B$ in the complex c plane showing the general pattern of the characteristic exponents for a one-mode truncation at $a = \pi, q = 0.8$ and $\epsilon = 0.45$.

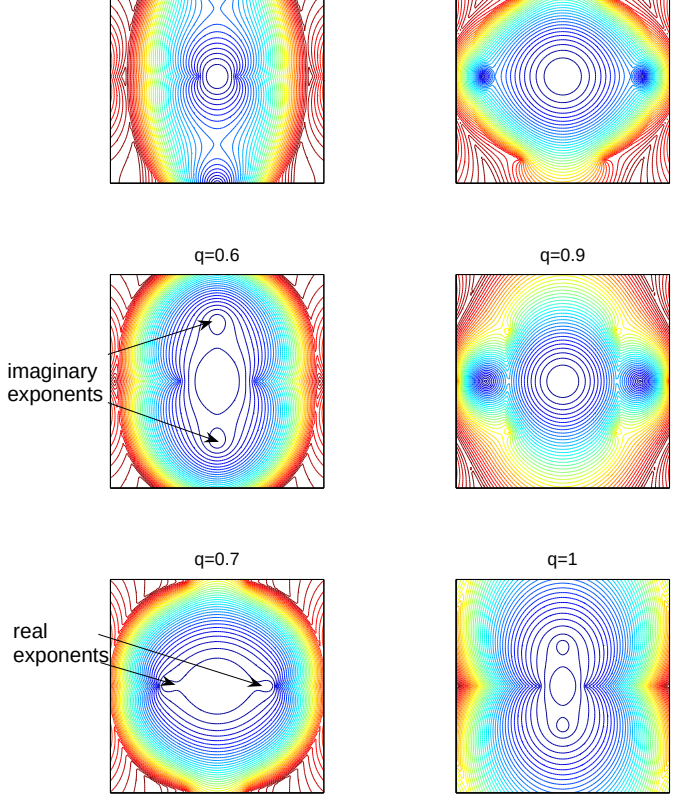

Figure 7: Contour plots of λ_B in the complex c plane for $-0.5 < \mathrm{Re}(c) < 0.5, -0.5 < \mathrm{Im}(c) < 0.5$ showing the location of the characteristic exponents near the origin for $a = \pi, \epsilon = 0.45$ and values of the wavenumber q in the range 0.5 to 1.

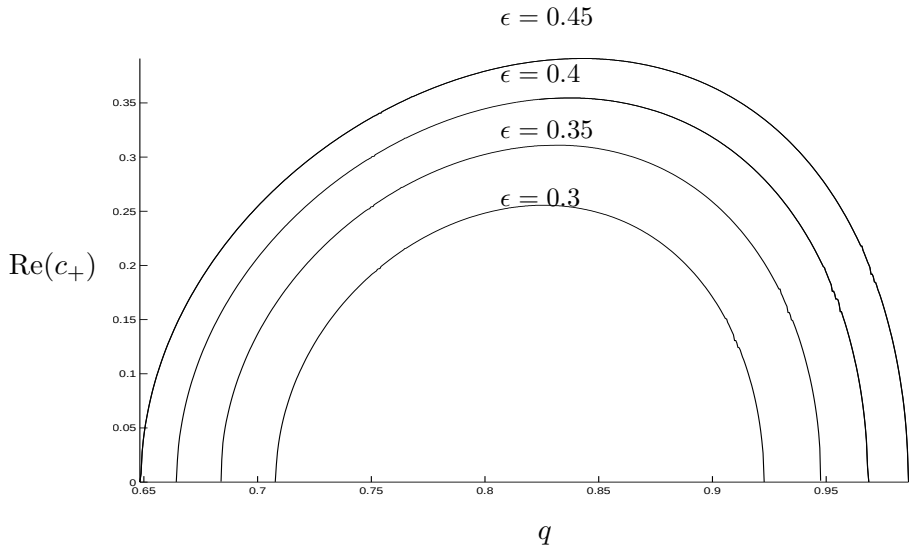

Figure 8: Variation of the characteristic exponent c_+ with wavenumber q for $a = \pi$ and $\epsilon = 0.3, 0.35, 0.4$ and 0.45.

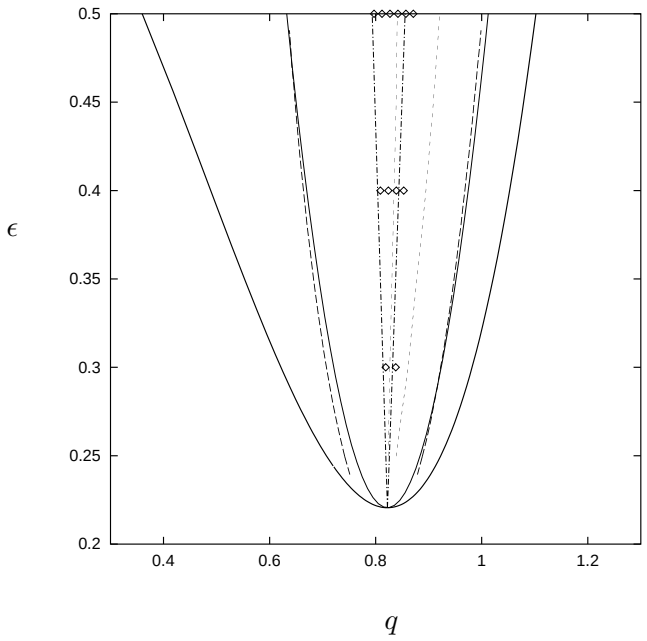

Figure 9: The q, ϵ plane for $a = \pi$ showing the marginal stability curve (heavy solid line) and the Eckhaus stability boundary based on weakly nonlinear theory (thin solid line) and numerical computation $(- - -)$. Also shown (see section 4) are the waveband for a semi-infinite channel based on a Floquet approximation $(\cdots)$, numerical computation $(\diamond\diamond\diamond)$ and weakly nonlinear theory $(- \cdot - \cdot -)$.

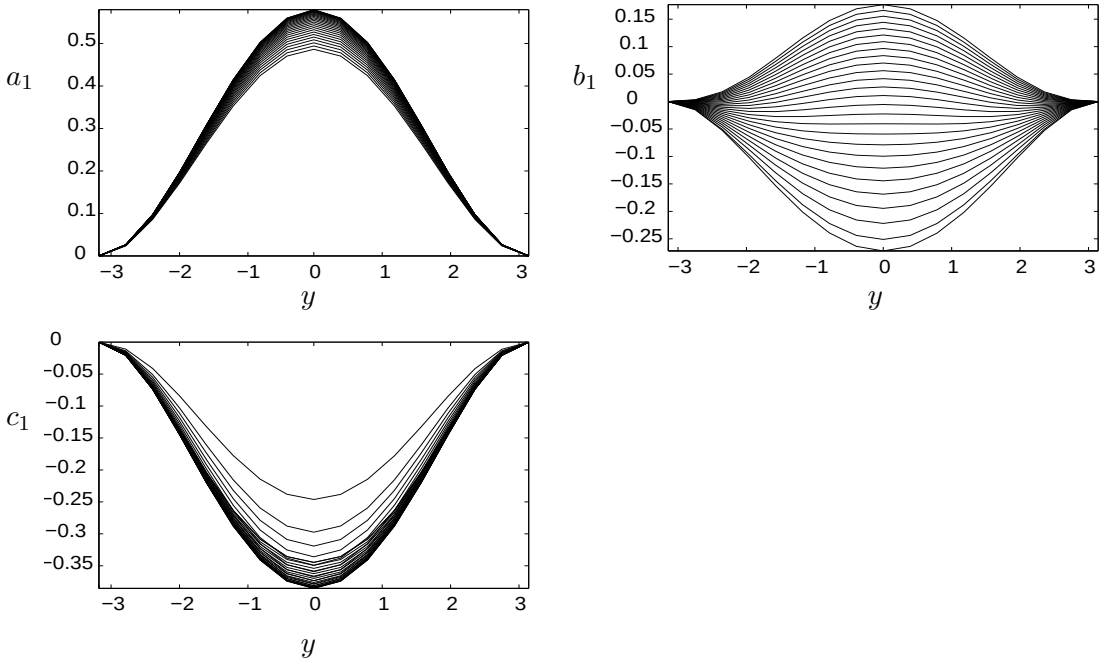

Figure 10: Coefficients $a_1(y), b_1(y)$ and $c_1(y)$ for wavenumbers in the range $0.824 < q < 0.954$ for $a = \pi$ and $\epsilon = 0.4$.

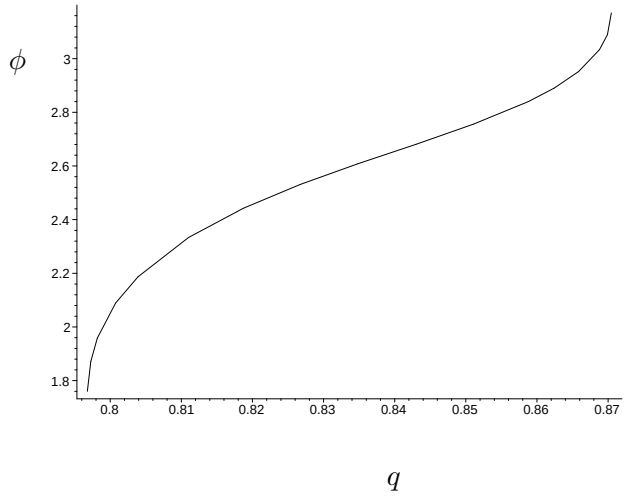

Figure 11: Phase shift ϕ as a function of wavenumber q for $a = \pi$ and $\epsilon = 0.5$.

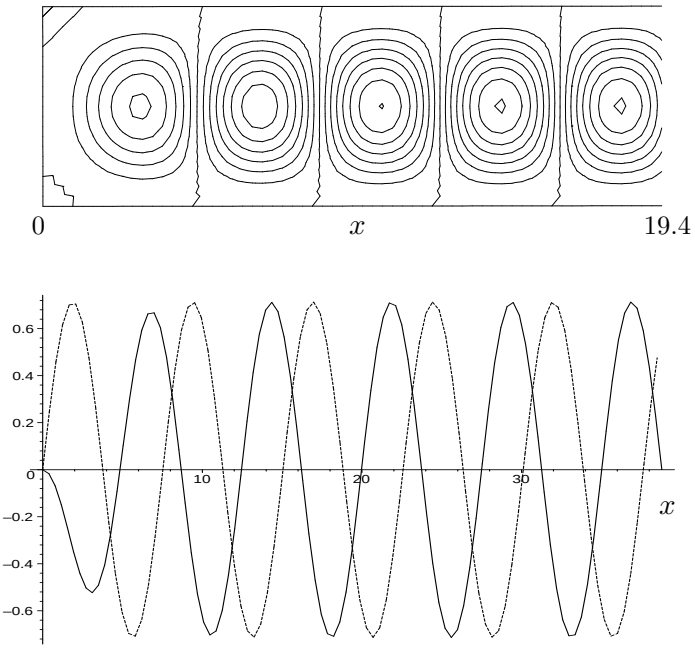

Figure 12: Contours of the steady-state solution $u(x, y)$ for $a = \pi, \epsilon = 0.5$ and $q = 0.835$. Also shown are $u(x, 0)$ and the corresponding periodic form $u_p(x, 0)$.

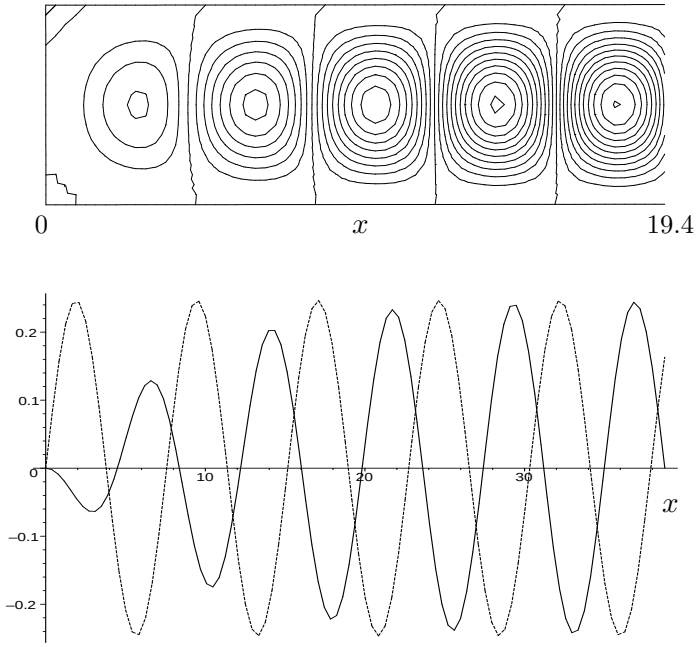

Figure 13: Contours of the steady-state solution $u(x, y)$ for $a = \pi, \epsilon = 0.25$ and $q = 0.829$. Also shown are $u(x, 0)$ and the corresponding periodic form $u_p(x, 0)$.

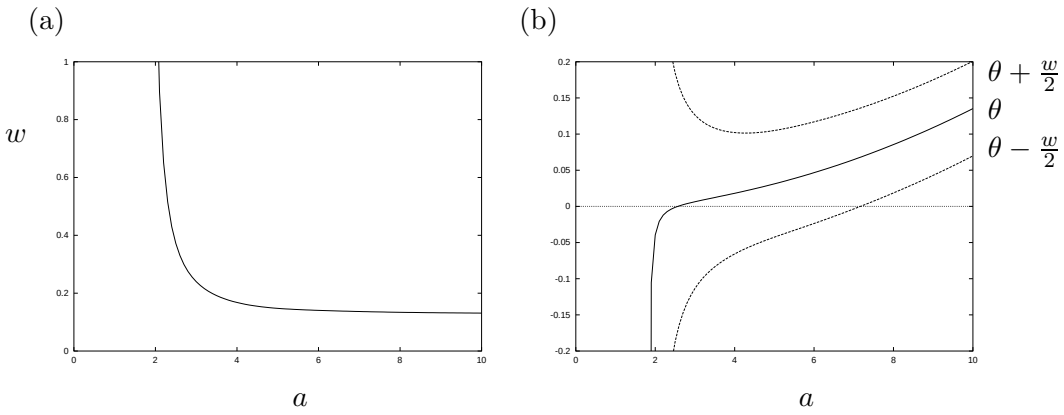

Figure 14: The wavelength selection parameters as a function of a: (a) w, (b) θ (—) and the waveband limits $\theta \pm \frac{w}{2}$ ($- - -$).

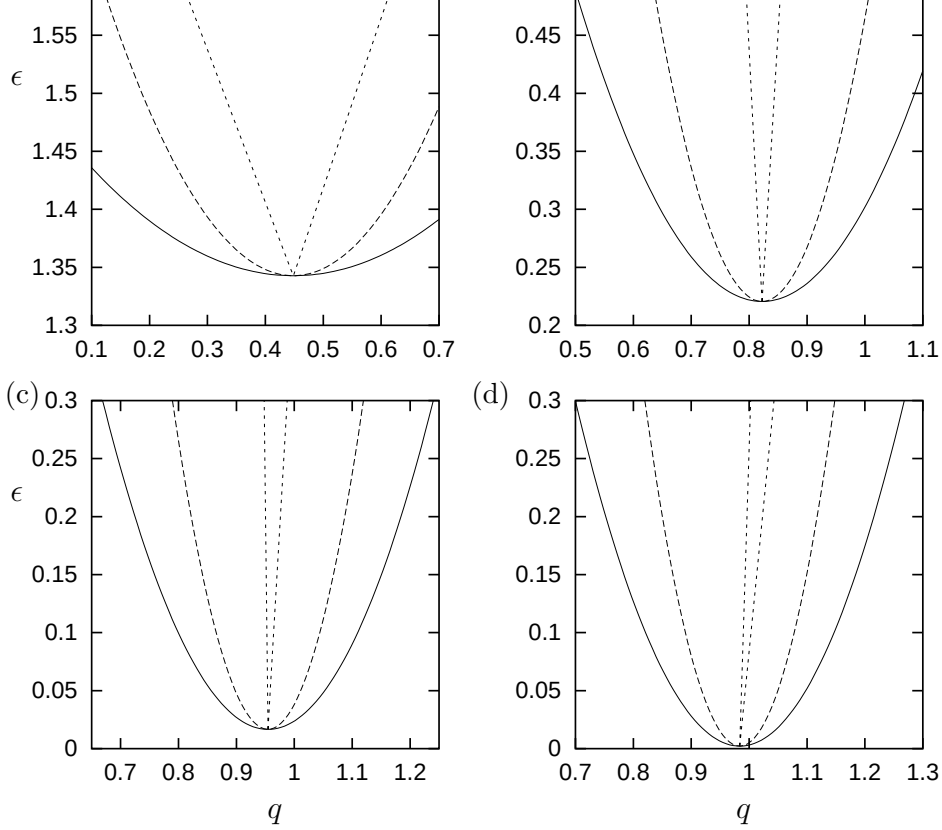

Figure 15: Weakly nonlinear results for the marginal stability curve (—), the Eckhaus boundary (- - -) and the restriction on the waveband imposed by the end wall at $x = 0$ ($\cdots$): (a) $a = 2$, (b) $a = \pi$, (c) $a = 6$, (d) $a = 10$.

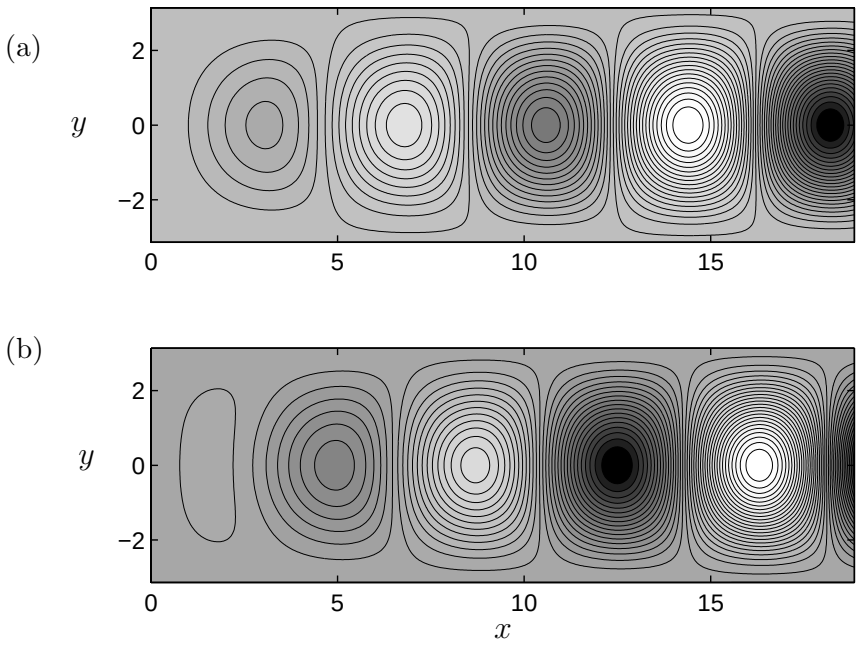

Figure 16: Contours of the inner solution U for $a = \pi$: (a) branch 1, corresponding to values of $s_{r,i}$ given by (67) with $\psi_0 = \gamma/2$, (b) branch 2, corresponding to values of $s_{r,i}$ given by (68) with $\psi_0 = \gamma/2$.

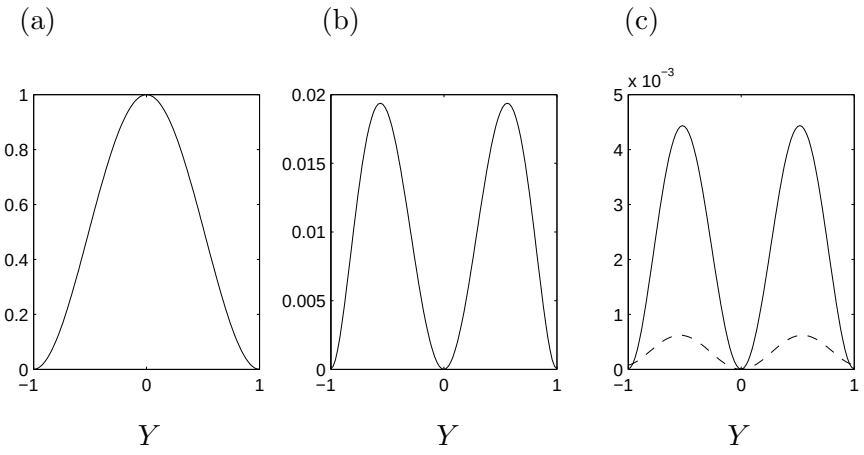

Figure 17: The functions (a) F_0, (b) G_0 and (c) H_1 (—) and H_3 (- - -).

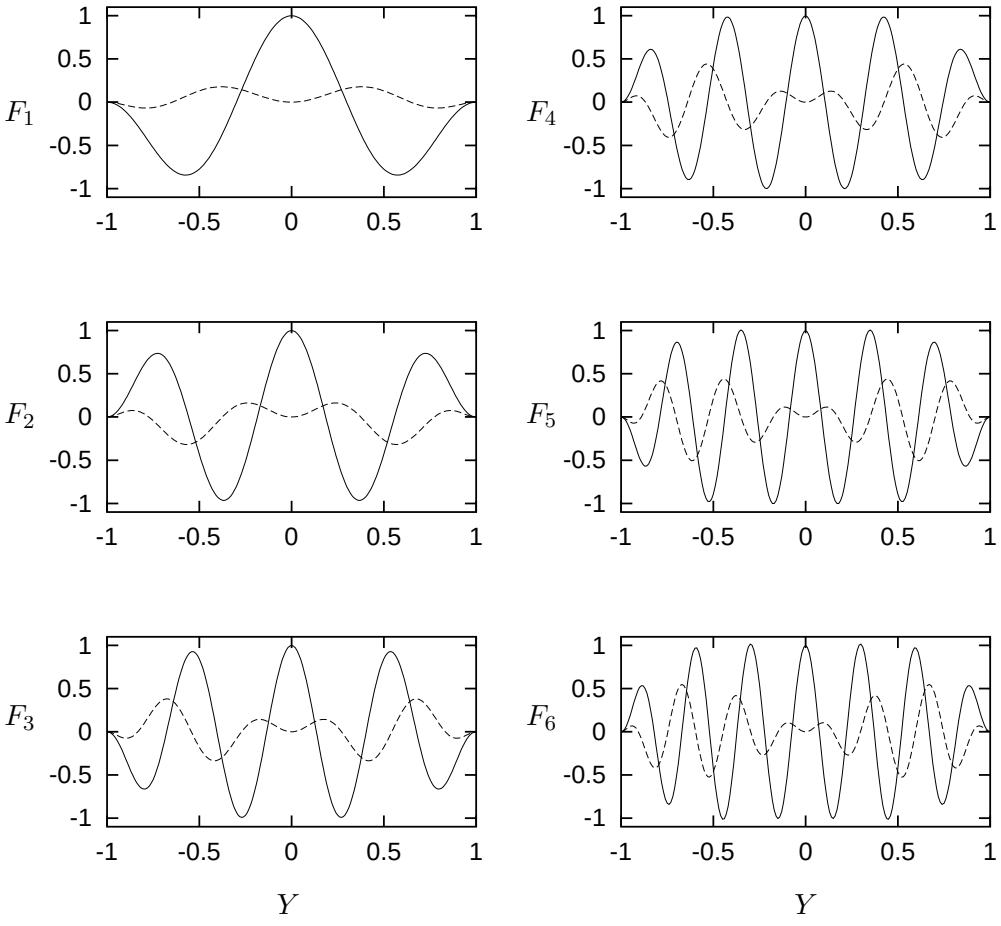

Figure 18: Real (—) and imaginary (- - -) parts of the six eigenfunctions $F_n, n = 1, \ldots 6$.